Ultramicroscopy 110 (2010) 626–633

Contents lists available at ScienceDirect

Ultramicroscopy

journal homepage: www.elsevier.com/locate/ultramic

Determination and simulation of nanoscale energy dissipation processes in amplitude modulation AFM

Carlos J. Gómez, Ricardo Garcia *

Instituto de Microelectrónica de Madrid SIC, Isaac Newton 8, 28760 Tres Cantos, Madrid, Spain

ARTICLE INFO

Keywords:
Phase imaging AFM
Amplitude modulation AFM
Energy dissipation
Force microscopy

ABSTRACT

We develop a theoretical framework that explains the use of amplitude modulation AFM to measure and identify energy dissipation processes at the nanoscale. The variation of the dissipated energy on a surface by a vibrating tip as a function of its amplitude has a shape that singles out the dissipative process. The method is illustrated by calculating the dynamic-dissipation curves for surface adhesion energy hysteresis, long-range interfacial interactions and viscoelastic processes. We also show that by diving the dissipated energy by its maximum value, the dynamic-dissipation curves become independent of the experimental parameters. In particular, for long-range dissipative processes we have derived an analytical relationship that shows the independence of the normalized dynamic-dissipation curves with respect the free amplitude, cantilever constant or quality factor.

1. Introduction

The development of an instrument that combines topography and compositional analysis is a goal of many nanoscale imaging techniques. In amplitude modulation atomic force microscopy (AM-AFM), the variation of the phase shift of the vibrating tip while imaging surface gives rise to a powerful source of compositional contrast in heterogeneous samples [1–19]. This method is usually known as *phase imaging* atomic force microscopy. Phase-imaging AFM is a versatile method to study material surfaces in their native environment and state with nanoscale spatial resolution. For experiments performed with high quality factor cantilevers (air), the variations observed in the phase shift signal are related to the amount of energy transferred from the tip to the sample surface (dissipation) [1,20–22]. As a consequence, phase shift variations carry information on the dissipative processes of the sample. In liquid or in bimodal AFM excitation schemes, the relationship between phase shifts and conservative and non-conservative forces is more complex and requires the inclusion of higher cantilever modes and/or harmonics [23–26].

The high spatial contrast derived from AFM phase images relies on the sensitivity of the phase shift to detect small variations of the dissipated energy. Energy dissipation can be studied from an atomistic [27,28] or a nanoscale perspective [29,30]. The latter emphasizes the quantitative relationship between dissipation and macroscopic quantities such as surface adhesion energy, elastic modulus, stiffness, plasticity index or viscoelasticity.

Here, we develop a theoretical model that explains the use of phase shifts in AM-AFM to measure and identify energy dissipation processes. We show that by normalizing the dissipated energy to its maximum value the method is practically independent from the experimental parameters such as the tip radius, force constant or quality factor. In particular, we develop an analytical expression that applies to dissipative processes that arise from long-range interactions. The agreement obtained between numerical simulations and the analytical expression validates the model. Finally, the theoretical method also supports the use of AM-AFM to obtain quantitative information on material properties.

2. Model

We have used a point-mass model to calculate the properties and interactions of a vibrating tip in the proximity of a surface. Point-mass models have demonstrated great quantitative accuracy to describe amplitude-modulation AFM experiments whenever the contribution of higher cantilever eigenmodes can be neglected [30–34]. The simulations were obtained by solving numerically the equation of motion with a fourth order Runge–Kutta algorithm.

The equation of motion in amplitude-modulation AFM is approximately described by

$$m\frac{d^2z}{dt^2} = -kz - \frac{m\omega_0}{Q}\frac{dz}{dt} + F_{ts} + F_0\cos\omega t \quad (1)$$

* Corresponding author.
E-mail address:rgarcia@imm.cnm.csic.es

0304-3991/$ - see front matter © 2010 Elsevier B.V. All rights reserved.
doi:10.1016/j.ultramic.2010.02.023

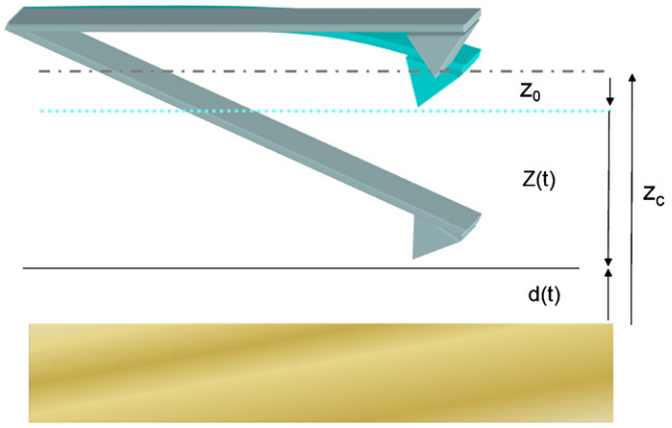

Fig. 1. Scheme of the different separations and spatial distances involved in AM-AFM. The average tip–surface separation z_c is the origin of the z coordinate. The instantaneous tip–sample separation is d; z is the instantaneous cantilever deflection and z_0 is the average cantilever deflection.

The total force that governs the tip motion includes the elastic response of the cantilever, the hydrodynamic damping with the medium, the tip–sample interaction force and the periodic driving force; Q, k and ω_0 are, respectively, the quality factor, the force constant and the angular resonant frequency of the free cantilever; F_0 and ω are, respectively, the amplitude and the angular frequency of the driving force. The steady-state oscillation of the above differential equation can be approximated by a sinusoidal oscillation $z(t)=z_c+A\cos(\omega t-\phi)$, where z_c, A and ϕ are, respectively, the average tip–sample separation, amplitude and phase shift of the oscillation with respect to the driving force (Fig. 1).

The tip–sample geometry is simulated by a semispherical tip and a flat sample. The tip–sample interaction contains long and short range forces. Long-range dissipative interfacial forces (non-contact) are calculated by using a time-dependent power law interaction:

$$F_{lr}=\frac{-\alpha(t)}{d^2} \tag{2}$$

where $\alpha=\alpha_a$ for $t\in[0,\ T/2]$ $\alpha=\alpha_r$ for $t\in(T/2,\ T]$. For separations $d\le a_0$, where a_0 is an intermolecular distance (0.165 nm), the resulting force is identified with the adhesion force given by the Dejarguin–Muller–Toporov (DMT) theory [35]:

$$F_{sh}=4\pi R\gamma=\frac{-\alpha}{a_0^2} \tag{3}$$

where γ is the surface energy and R the tip radius. In addition to the adhesion force, during the contact ($d\le a_0$), there is a repulsive force arising from Pauli and ionic repulsion. The repulsive force and the sample deformation are modeled by using the DMT contact mechanics:

$$F_{ts}=\frac{-\alpha}{a_0^2}+\frac{4}{3}E_{eff}\sqrt{R}\delta^{3/2} \tag{4}$$

where E_{eff} and δ are the effective elastic modulus and the indentation (deformation), respectively.

The viscoelastic force is calculated by combining the Voigt model for the viscoelastic response [36] and the Hertz contact mechanics model for the surface deformation [31]:

$$F_v=\eta\sqrt{R\delta}\frac{d\delta}{dt} \tag{5}$$

where η is the viscosity of the sample.

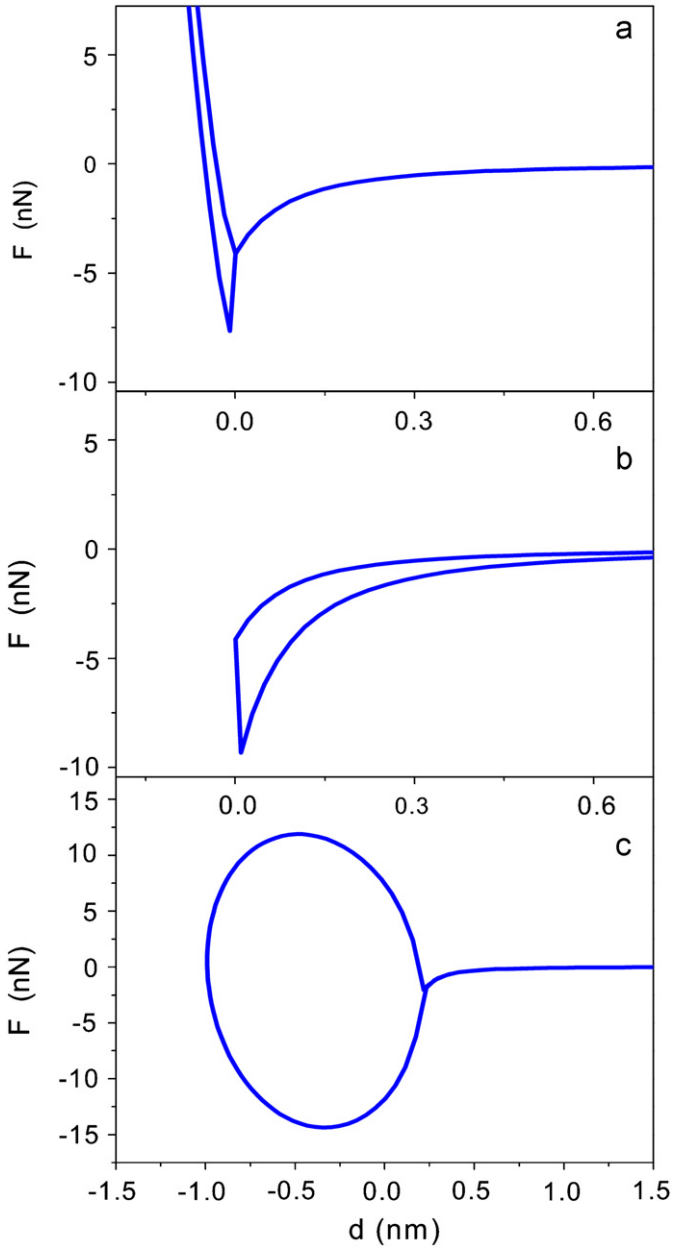

Fig. 2. Non-conservative tip–surface forces: (a) long-range surface adhesion hysteresis, (b) short-range surface adhesion hysteresis and (c) viscoelasticity.

Fig. 2 shows the above forces plotted versus the tip–sample distance. The hysteresis in the force curves illustrates the non-conservative nature of the interaction. The area enclosed by the hysteresis loop gives the amount of the energy dissipated on the sample surface.

3. Identification of energy dissipation processes

The sine of the phase lag that exists between the external excitation and the tip response is directly linked to the amount of energy dissipated on the sample [20]. In addition, there are several analytical relationships that relate the dissipated energy to some sample properties such as surface adhesion energy, elastic modulus, stiffness, plasticity index or viscoelasticity. It has also been shown that the representation of the dissipated energy

(dynamic-dissipation curves hereafter) and, in particular, its derivative with respect to the amplitude characterizes the dissipation process [22].

Here we study three different energy dissipation processes, surface energy hysteresis, dissipative interfacial interactions between non-contact surfaces and viscoelasticity. The results obtained from the numerical simulations show that the above dissipation processes have a unique type of dynamic-dissipation curve (Fig. 3). These observations are enhanced by taking the derivative of the dissipated energy.

For surface energy hysteresis and dissipative interfacial interactions between non-contact surfaces, the simulations have been performed with the following set of parameters (set 1) k=2 N/m, ω_0=59 kHz, Q=150 γ_a=33 mJ/m^2, $\Delta\gamma$=33 mJ/m^2, $\Delta\alpha=HR/4$, R=10 nm, $H=6.77\times10^{-20}$ J, η=0, E_{eff}=150 GPa. To simulate the viscoelastic process the parameters used (set 2) were k=40 N/m, ω_0=300 kHz, Q=500, R=10 nm, γ_a=20 mJ/m^2, $\Delta\gamma$ =0, $\Delta\alpha$ =0, η=800 Pa s, E_{eff}=500 MPa. Here H is the Hamaker constant, γ_a the surface energy when the tip approaches the surface and $\Delta\gamma$ the difference in the surface energy between approaching and retracting curves, i.e., the surface energy hysteresis in a cycle; $\Delta\alpha=\alpha_r-\alpha_a$ is the hysteresis in the long range attractive force (Eq. (3)).

3.1. Long-range surface adhesion hysteresis

The dissipated energy per cycle in the presence of long-range adhesion hysteresis (Eq. 2) can be calculated by

$$E_{dis}=\oint\frac{\alpha}{z^2}dz=\int_{d_1}^{d_2}\frac{\alpha_a}{z^2}dz-\int_{d_2}^{d_1}\frac{\alpha_r}{z^2}dz=\Delta\alpha\left(\frac{1}{d_1}-\frac{1}{d_2}\right) \tag{6}$$

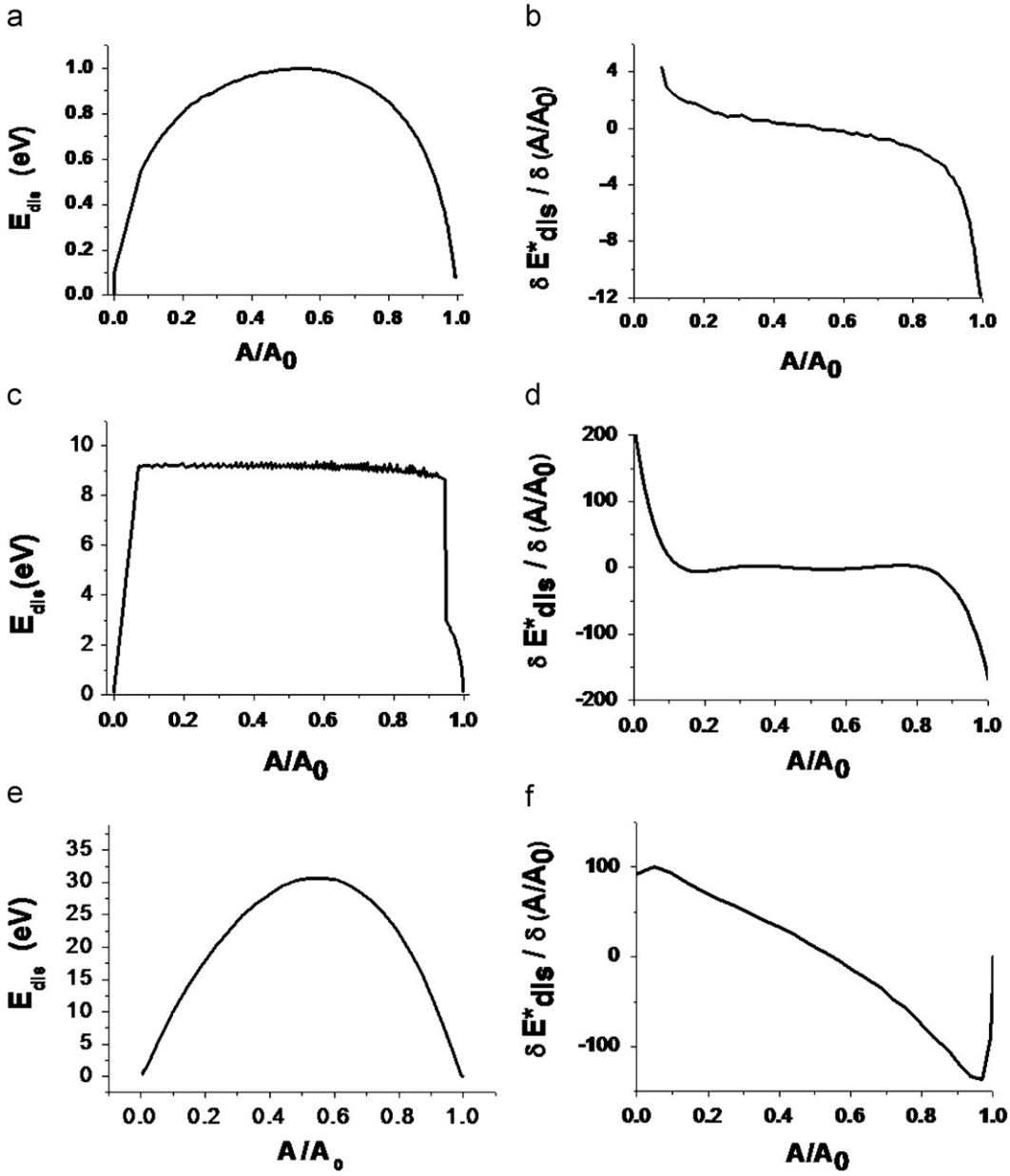

Fig. 3. Dynamic-dissipation curves for different non-conservative tip–surface forces. Energy dissipation and its derivative as a function of the amplitude ratio for long-range surface adhesion hysteresis (a, b), short-range surface adhesion hysteresis (c, d), and viscoelasticity (e, f).

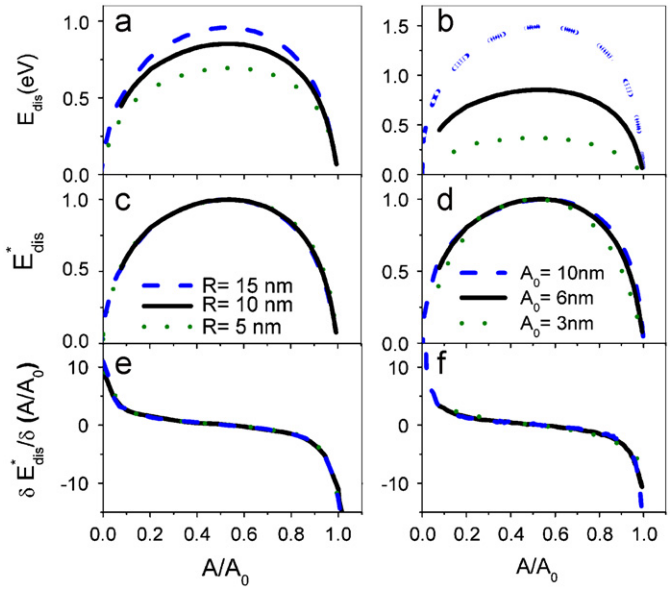

Fig. 4. Dynamic-dissipation curves for long-range dissipative forces. Dissipation (a, b), normalized dissipation (c, d), and derivate (e, f) as a function of the amplitude ratio for long-range dissipative forces. The left-hand column represents a simulation for A_0=6 nm and three different tip radii (5, 10 and 15 nm). The right-hand column is for R=10 nm and three different free amplitudes (3, 6 and 10 nm).

where d_1 and d_2 are the closest and the farthest tip–surface gap separations during the cycle, respectively. The parameters used in the simulations were chosen to model a silicon oxide sample and a vibrating tip in the attractive regime. The dynamic-dissipation curves plotted for different tip radii and free amplitudes are shown in Fig. 4. In all the cases, the dissipated energy shows a maximum with respect to the amplitude ratio. As expected, for a fixed amplitude, the dissipated energy decreases with the radius (Fig. 4a). Similarly, for a fixed radius, the dissipated energy decreases by decreasing the free amplitude (Fig. 4b). By normalizing the energy to its maximum ($\overline{E_{dis}} = E_{dis}/E_{dis}$ (max)), we found that the dynamic-dissipation curves are independent of the experimental parameters (Fig. 4c and d). The derivative is characterized by a region where the derivative changes very slowly. This region is flanked by sharp increases at both ends of the amplitude ratio interval.

Fig. 5 shows the dynamic-dissipation curves for cantilevers with different force constants. Each contour line traces a line of equal dissipated energy. Fig. 5a shows that the dissipated energy increases with the free amplitude (k=2 N/m and Q=150). However, the dynamic-dissipation curves of the normalized dissipated energy do not depend on the free amplitude values (Fig. 5b). Fig. 5c shows that the dissipated energy increases with the force constant because the energy stored in the cantilever is proportional to k. Again by normalizing the energy to its maximum value, the dynamic-dissipation curves become

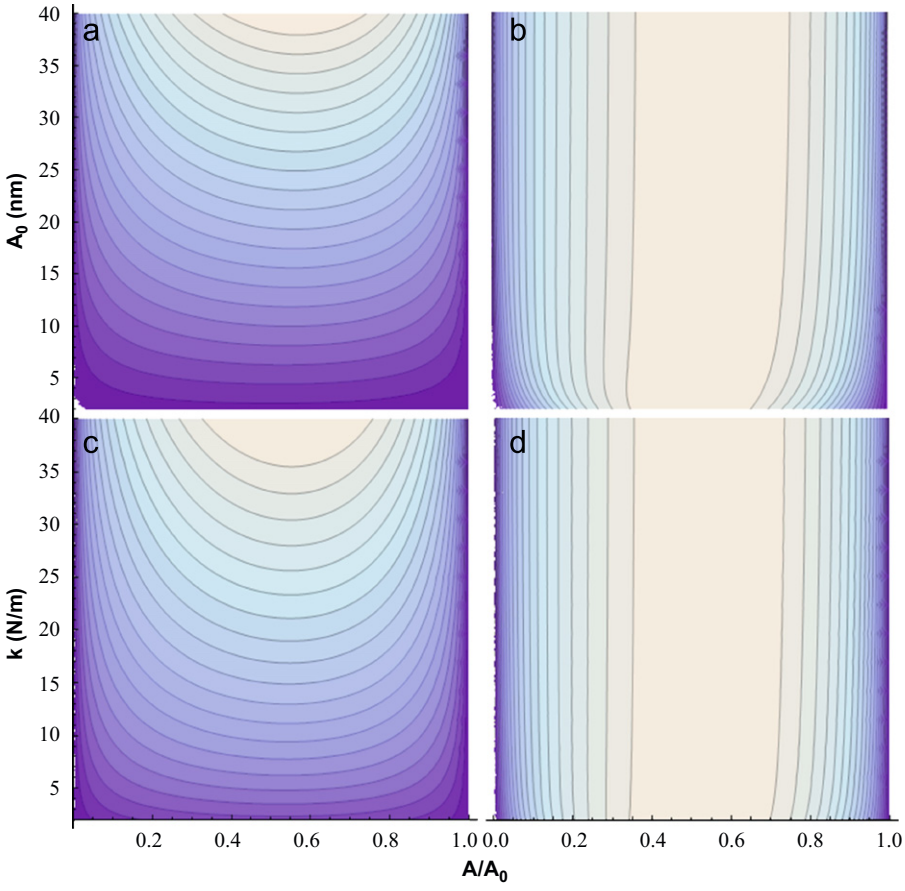

Fig. 5. Dynamic-dissipation curves as a function of the free amplitude and force constant. The contour line traces a line of equal dissipated energy: (a) dissipation and (b) normalized dissipation for different free amplitude values (k=2 N/m). (c) Dissipation and (d) normalized dissipation for different force constants (A_0=5 nm). The contour lines for the normalized dissipated energy do not depend on the experimental parameters (vertical lines).

independent of the cantilever constant (Fig. 5d). In Fig. 5a and c, the dissipated energy increases from bottom to top. Similar results are obtained when the Q factor is changed. The above results have been obtained by using Eq. (A.10) of the appendix with the following parameters: A_0=5 nm, R=10 nm, Q=150, k=2 N/m and $\Delta\alpha$=HR/4.

3.2. Short-range surface adhesion hysteresis

Upon contact, the energy might also be dissipated by short range forces due to the presence of adhesion hysteresis. Similarly, the dissipated energy is calculated by

$$E_{dis} = \oint 4\pi R\gamma\, dz = 4\pi R \int_{d_1}^{d_2} \gamma_a\, dz - \int_{d_2}^{d_1} \gamma_r\, dz = 4\pi R\Delta\gamma \qquad (7)$$

Fig. 6 shows the energy dissipated by short range forces for different amplitudes and tip radii. For a fixed free amplitude, the dissipation increases with the radius (5, 7 and 10 nm) because the adhesion hysteresis also increases with the tip's radius (Fig. 6a). An increase of the free amplitude from 20 to 60 nm produces a small increase in the dissipated energy (from 9 to 10 eV). This is due to the small differences that for stiff materials (E_{eff}=150 GPa in this case) exist between the indentation values for both amplitudes. Again, the normalization with respect the maximum value of the dissipated energy produces the overlapping of the above curves (Fig. 6c and d). Finally, by taking the derivative of the energy with respect to the amplitude the independence of the curves with respect to the experimental parameters is enhanced (Fig. 6e and f).

3.3. Viscoelasticity

To simulate the viscoelastic response of the sample we use a model that combines Voigt's viscoelastic response with the surface deformation given by the Hertz contact mechanics [21,22]. This model gives the force described in Eq. (5). The dynamic-dissipation curves corresponding to the above force has been calculated for different values of the viscosity (Fig. 7a). By normalizing the energy it is found that the curves do not depend on the actual value of the viscosity (Fig. 7b and c).

3.4. Multiple dissipation processes

We have also simulated a more general tip–surface interaction that includes the three dissipation process described above. This

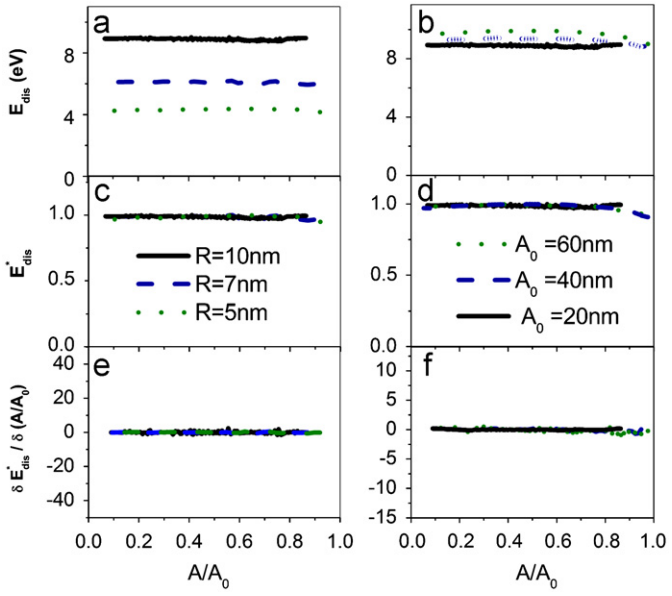

Fig. 6. Dynamic-dissipation curves for a short-range dissipative force: (a) dissipation (b) normalized dissipation, (c) derivate for A_0=20 nm and radii (5, 7 and 10 nm). (d) Dissipation (e) normalized dissipation, (f) derivate for R=10 nm and three free amplitudes (20, 40 and 60 nm).

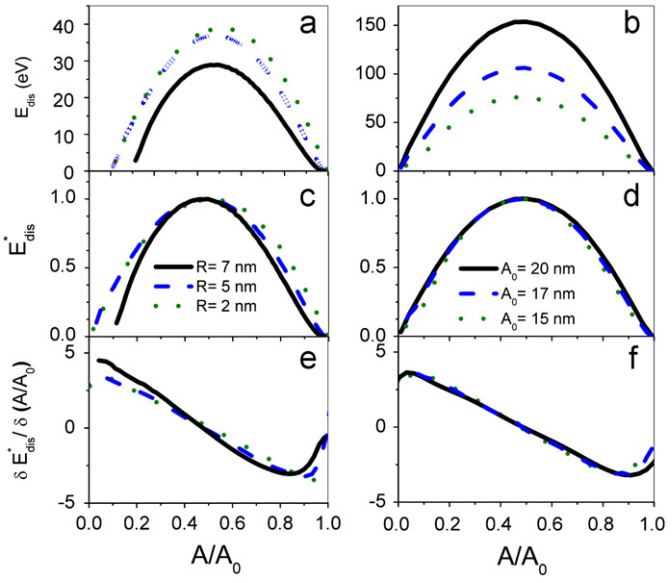

Fig. 8. Dynamic-dissipation curves for a tip–surface interaction that includes several dissipation processes: (a) dissipation, (b) normalized dissipation, (c) first derivative for A_0=10 nm and radii (2, 5 and 7 nm), (d) dissipation, (e) normalized dissipation and (f) first derivative for R=10 nm and three free amplitudes (15, 17, 20 nm).

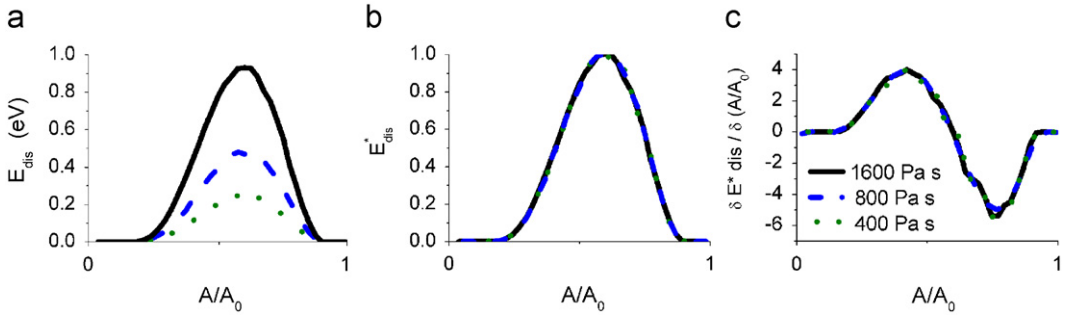

Fig. 7. Dynamic-dissipation curves for a viscoelastic force: (a) dissipation, (b) normalized dissipation and (c) derivative as function of the amplitude ratio for different viscosity values (400, 800, 1600 Pa s).

case could correspond to imaging a soft polymer surface. For this interaction, the dynamic-dissipation curves reflect the contribution of the three dissipative processes. Depending on the values of the parameters, one process might dominate over the other two and then the dynamic-dissipation curves will be similar to the ones of the dominating process. The corresponding dynamic-dissipation curves as a function of the free amplitude are shown in Fig. 8a, c and d while Fig. 8b, d and f shows the dependence on the tip radius. We have used the parameters described in set 2 but with $\Delta\gamma$=33 mJ/m^2 and $\Delta\alpha$=HR/4. The dynamic-dissipation curves indicate that viscoelasticity and long-range surface adhesion are the dominant contributions.

4. Discussion

The results presented in the previous sections have revealed some remarkable features such as the existence of a maximum in the dissipated energy, the dependence of the dynamic-curve on the dissipation process or the near independence of the dynamic-dissipation values (normalized energy) on the tip radius, the free amplitude or the cantilever constant.

We start by explaining the origin of the maximum observed in the dynamic dissipation curves in the presence of long-range adhesion hysteresis (Fig. 4). This maximum is related to existence of a minimum in the tip–surface distance. The existence of such a minimum implies a maximum in the dissipated energy because the dissipated energy is calculated by integrating the force (approach and retraction) between the closest and farthest tip–surface distances (Eq. (6)). The lower limit is precisely the more relevant because the forces and the force differences are larger at the closest tip–surface distance. Fig. 9a shows the existence of a minimum tip–surface distance as a function of the amplitude ratio. The simulations have been performed for both elastic and non-conservative interactions.

The maximum observed in the presence of viscoelastic interactions has a similar explanation. The simulations show the presence of a maximum in the indentation as a function of the amplitude ratio (Fig. 9c). The amplitude ratio at which the indentation has a maximum coincides with the amplitude ratio that gives the maximum in the dynamic-dissipation curves.

The dynamic-dissipation curves of the normalized energy show a very small dependence on the tip radius, the force constant or the free amplitude. This suggests that their influence on the dissipated energy can be factorized independently from the dependence on the amplitude ratio. In fact, we have derived an analytical expression for the dissipated energy that applies for long-range dissipative forces that supports the above results. In the appendix we deduce

$$E_{dis} = C\sqrt[3]{\bar{A}\left(1-\bar{A}^2\right)} \tag{8}$$

where

$$C = \sqrt[3]{\frac{8\Delta\alpha^3 k^2 A_0^3}{(\alpha_a+\alpha_r)^2 Q^2}} = \Delta\alpha A_0 \sqrt[3]{\frac{8k^2}{(\alpha_a+\alpha_r)^2 Q^2}} \approx E_{dis}(\max) \tag{9}$$

then

$$\overline{E_{dis}} = \frac{E_{dis}}{E_{dis}(\max)} = \sqrt[3]{\bar{A}\left(1-\bar{A}^2\right)} \tag{10}$$

5. Conclusions

We develop a theoretical framework that explains the use of phase shifts in amplitude modulation AFM to measure and identify energy dissipation processes. The method requires the determination of the energy dissipated on the sample surface as a function of the amplitude while the tip approaches towards the surface. The representation of the dissipated energy and, in particular, its derivative with respect to the amplitude ratio characterizes the dissipation process. Those curves are called dynamic-dissipation curves. Surface energy hysteresis, viscoelasticity and long-range dissipative interfacial interactions processes have been studied. The numerical simulations show that the dynamic-dissipation curves (normalized) are practically independent of some experimental parameters such as the tip radius, force constant or quality factor. Specifically, for long-range dissipative processes, we have derived an analytical relationship that supports the independence of the normalized dynamic-dissipation curves with the experimental parameters.

A more general tip–surface interaction could involve the contribution of several non-conservative processes. The simulations show that the resulting dynamic-dissipation curves could be considered a combination of the individual dissipative processes. This, in turns, enable us to separate each respective contribution.

Acknowledgments

This work was financially supported by the MICINN (Spain) (MAT2006-03833; MAT2009-08650) and the Comunidad de Madrid (Nanobio-M, S0505/MAT-0283).

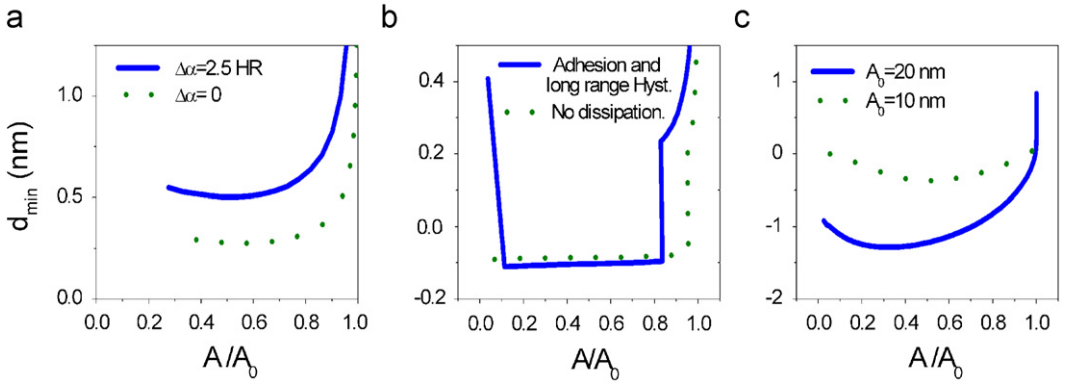

Fig. 9. Minimum tip–surface distance curves for different tip–surface interactions: (a) Short-range forces with (solid line) and without (dotted line) dissipation; A_0=10 nm, R=10 nm. (b) Long-range forces with (solid line) and without (dotted line) dissipation; A_0=20 nm, R=10 nm. (c) Viscoelastic process for two values of A_0.

Appendix

In the following, we derive an analytical expression for the dependence of the dissipated energy on the amplitude ratio. The dissipated energy can be obtained integrating the non-conservative force over one period. In particular, for a non-conservative force given by $F_{dis}=\alpha(t)/z^2$ [23] where the strength of the force depends on the direction of the tip movement:

$$E_{dis}=\oint F_{nc}\,dz=\Delta\alpha\left(\frac{1}{d_1}-\frac{1}{d_2}\right)=\frac{2\Delta\alpha A_0\overline{A}}{(z_c+z_0)^2-\overline{A}^2A_0^2}=\frac{2\Delta\alpha A_0\overline{A}}{L} \quad (A.1)$$

where $\alpha(t)$ is a function that varies with time in a step-like manner; $\alpha=\alpha_a$ when the tip is approaching towards the sample, and $\alpha=\alpha_r$ when is retracting from the sample. $\overline{A}$ is the amplitude ratio $\overline{A}=A/A_0$; d_1 and d_2 are, respectively, the maximum and minimum tip–sample distance defines as $d_1=z_c+z_0+A$ and $d_2=z_c+z_0-A$; L is the product of the above distances.

Alternatively, the dissipated energy could be obtained by expressing the non-conservative force in terms of the other forces and integrating over one period:

$$E_{dis}=\oint F_{nc}\,dz=\int_0^T(m\ddot{z}+b\dot{z}+kz-F\cos\omega t-F_c)\dot{z}\,dt$$
$$=\frac{\pi kA_0^2}{Q}\left(\overline{A}\sin\phi-\overline{A}^2\right) \quad (A.2)$$

In addition, the virial theorem can be used to derive a complementary expression that links the phase shift with the average force per period "F_{ts}" and the virial of the force "$F_{ts}z$" [31]:

$$\cos\phi=\frac{2Q}{k\overline{A}A_0^2}\left[\frac{\langle F_{ts}{}^2\rangle}{k}-\langle F_{ts}z\rangle\right] \quad (A.3)$$

On the other hand,

$$F_{ts}=\frac{1}{T}\oint F_{ts}\,dt=-\frac{(\alpha_a+\alpha_r)}{2}\frac{z_c+z_0}{\left[(z_c+z_0)^2-\overline{A}^2A_0^2\right]^{3/2}}=-\frac{(\alpha_a+\alpha_r)}{2}\frac{z_c+z_0}{L^{3/2}} \quad (A.4)$$

$$\langle F_{ts}z\rangle=\frac{1}{T}\oint F_{ts}z\,dt=\frac{(\alpha_a+\alpha_r)}{2}\frac{\overline{A}^2A_0^2}{\left[(z_c+z_0)^2-\overline{A}^2A_0^2\right]^{3/2}}$$
$$=\frac{(\alpha_a+\alpha_r)}{2}\frac{\overline{A}^2A_0^2}{L^{3/2}}=-\frac{\overline{A}^2A_0^2}{z_c+z_0}\langle F_{ts}\rangle \quad (A.5)$$

In many experimental situations, the mean deflection of the cantilever is negligible with respect to the amplitude ($z_0\ll\overline{A}A_0$), then by substituting Eqs. (A.3)–(A.5) into Eq. (A.2), we obtain,

$$E_{dis}=\frac{\pi kA_0^2\overline{A}}{Q}\left[-\overline{A}+\sqrt{1-\left\{\frac{2Q}{kA_0^2\overline{A}}\langle F_{ts}z\rangle\right\}^2}\right]$$
$$=\frac{\pi kA_0^2\overline{A}}{Q}\left[-\overline{A}+\sqrt{1-\frac{\overline{A}^2}{L^3}\left\{\frac{Q(\alpha_a+\alpha_r)}{k}\right\}^2}\right] \quad (A.6)$$

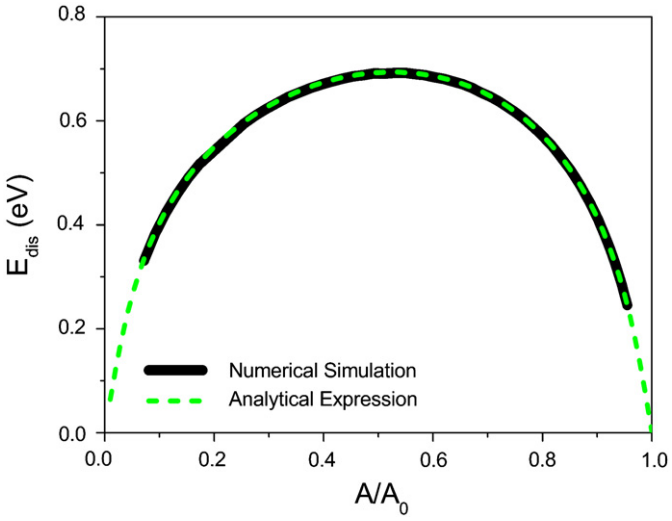

Fig. 10. Comparison between numerical simulations (solid line) and the analytical solution described by Eq. (A.10) (dashed line). For a long-range interfacial dissipative force.

By combining (A.1) and (A.6) we deduce an equation that relates the dissipated energy with the amplitude ratio ($\overline{A}$),

$$\frac{E_{dis}^3}{3N\overline{A}}+S^2\frac{E_{dis}^2}{\overline{A}^2}+2SE_{dis}+\left(\overline{A}^2-1\right)=0 \quad (A.7)$$

with

$$N=\frac{8\Delta\alpha^3k^2A_0^3}{3(\alpha_a+\alpha_r)^2Q^2} \quad (A.8)$$

$$S=\frac{Q}{\pi kA_0^2} \quad (A.9)$$

The real solution of the above third order equation gives

$$E_{dis}=\frac{N}{A}\left[I(\overline{A})+\frac{S^4-2S\overline{A}^3/N}{I(\overline{A})}-S^2\right] \quad (A.10)$$

where

$$I(\overline{A})=\sqrt[3]{\frac{1}{N^2}\left[3\overline{A}^3S^3N-\frac{3}{2}\overline{A}^4\left(\overline{A}^2-1\right)-S^6N^2+\overline{A}^2\sqrt{\frac{9}{4}\overline{A}^4\left(\overline{A}^2-1\right)^2-\overline{A}^3\left(\overline{A}^2-9\right)S^3N-3S^6N^2}\right]} \quad (A.11)$$

The curves obtained with numerical simulations and the values given by using Eq. (A.10) are in very good agreement (Fig. 10). This validates the analytical expression.

A more simplified expression can be obtained by assuming that $A_0>4$ nm, $k>2$ N/m and $R>3$ nm, then

$$E_{dis}=\sqrt[3]{3N\overline{A}\left(1-\overline{A}^2\right)}=C\sqrt[3]{\overline{A}\left(1-\overline{A}^2\right)} \quad (A.12)$$

$$E_{dis}^*=\frac{E_{dis}}{E_{dis}(\max)}=\sqrt[3]{\overline{A}\left(1-\overline{A}^2\right)} \quad (A.13)$$

where

$$C=\sqrt[3]{3N} \quad (A.14)$$

Eq. (A.13) reproduces the result given by the numerical simulations, that is, the normalization curves render a unique dynamic-dissipation curve. We have estimated that 10% maximum error in the values given by Eq. (A.13) with respect to those given by (A.10).

References

[1] R. Garcia, R. Magerle, R. Perez, Nanoscale compositional mapping with gentle forces, Nat. Mater. 6 (2007) 405–411.
[2] D.A. Chernoff, in: G.W. Bailey et al.(Ed.), Proceedings of the Microscopy and Microanalysis, Jones & Begell, New York, 1995, pp. 888–889.
[3] J. Tamayo, R. García, Deformation, contact time, and phase contrast in tapping mode scanning force microscopy, Langmuir 12 (1996) 4430.
[4] S.N. Magonov, V. Elings, V.S. Papkov, AFM study of thermotropic structural transitions in poly (diethylsiloxane), Polymer 38 (1997) 297–307.
[5] G. Reiter, G. Castelein, J.U. Sommer, A. Röttele, T. Thurn-Albrecht, Direct visualization of random crystallization and melting in arrays of nanometer-size polymer crystals, Phys. Rev. Lett. 87 (2001) 226101.
[6] A. Knoll, K.S. Lyakhova, A. Horvat, G. Krausch, G.J.A. Sevink, A.V. Zvelindovsky, R. Magerle, Direct imaging and mesoscale modeling of phase transitions in a nanostructured fluid, Nat. Mater. 3 (2004) 886.
[7] N. Rehse, S. Marr, S. Scherdel, R. Magerle, Three-dimensional imaging of semi crystalline polypropylene with 10 nm resolution, Adv. Mater. 17 (2005) 2203–2206.
[8] L. Tsarkova, A. Knoll, R. Magerle, Rapid transitions between defect configurations in a block copolymer melt, Nano Letters 6 (2006) 1574.
[9] J. Xu, B.H. Guo, Z.M. Zhang, J.J. Zhou, Y. Jiang, S. Yan, L. Li, Q. Wu, G.Q. Chen, J.M. Schultz, Direct AFM observation of crystal twisting and organization in banded spherulites of chiral poly(3-hydroxybutyrate-*co*-3-hydroxyhexanoate), Macromolecules 37 (2004) 4118.
[10] H. Bodiguel, H. Montes, C. Fretigny, Depth sensing and dissipation in tapping mode atomic force microscopy, Rev. Sci. Instrum. 75 (2004) 2529–2535.
[11] W. Wu, K. Matyjaszewski, T. Kowalewski, Monitoring surface thermal transitions of ABA triblock copolymers with crystalline segments using phase contrast tapping mode atomic force microscopy, Langmuir 21 (2005) 1143–1148.
[12] Z. Suo, X. Yang, R. Avci, L. Kellerman, D.W. Pascual, M. Fries, A. Steele, HEPES-stabilized encapsulation of *Salmonella typhimurium*, Langmuir 23 (2007) 1365.
[13] R. Garcia, J. Tamayo, M. Calleja, F. Garcia, Phase contrast in tapping-mode scanning force microscopy, Appl. Phys. A 66 (1998) S309–S312.
[14] R.V. Martínez, F. Garcia, R. Garcia, E. Coronado, A. Forment-Aliaga, F.M. Romero, S. Tatay, Nanoscale deposition of single-molecule magnets onto SiO_2 patterns, Adv. Mater. 19 (2007) 291.
[15] W.S. Xu, P.M. Wood-Adams, C.G. Robertson, Measuring local viscoelastic properties of complex materials with tapping mode atomic force microscopy, Polymer 47 (2006) 4798–4810.
[16] A. Checco, Y. Cai, O. Gang, B.M. Ocko, High resolution non-contact AFM imaging of liquids onto chemically nanopatterned surfaces, Ultramicroscopy 106 (2006) 703–708.
[17] J. Baltrusaitis, V.H. Grassian, Calcite (1014) surface in humid environments, Surf. Sci. 603 (2009) L99–L104.
[18] J. Melcher, C. Carrasco, X. Xu, J.L. Carrascosa, J. Gómez-Herrero, P.J. de Pablo, A. Raman, Origins of phase contrast in the atomic force microscope in liquids, Proc. Natl. Acad. Sci. USA 106 (2009) 13655–13660.
[19] J.J. Kuna, K. Voïtchovsky, C. Singh, H. Jiang, S. Mwenifumbo, P.K. Ghorai, M.M. Stevens, S.C. Glotzer, F. Stellacci, The effect of nanometre-scale structure on interfacial energy, Nat. Mater. 8 (2009) 837–842.
[20] B. Anczykowski, B. Gotsmann, H. Fuchs, J.P. Cleveland, V.B. Elings, How to measure energy dissipation in dynamic mode atomic force microscopy, Appl. Surf. Sci. 140 (1999) 376.
[21] N.F. Martinez, R. Garcia, Measuring phase shifts and energy dissipation with amplitude modulation atomic force microscopy, Nanotechnology 17 (2006) S167–S172.
[22] R. Garcia, C.J. Gomez, N.F. Martinez, S. Patil, C. Dietz, R. Magerle, Identification of nanoscale dissipation processes by dynamic atomic force microscopy, Phys. Rev. Lett. 97 (2006).
[23] J. Tamayo, Energy dissipation in tapping-mode scanning force microscopy with low quality factors, Appl. Phys. Lett. 75 (1999) 3569–3571.
[24] J. Melcher, X. Xu, A. Raman, Multiple impact regimes in liquid environment dynamic atomic force microscopy, Appl. Phys. Lett. 93 (2008) 093111.
[25] J. Melcher, C. Carrasco, X. Xu, Origins of phase contrast in the atomic force microscope in liquids, Proc. Natl. Acad. Sci. USA 106 (2009) 13655–13660.
[26] J.R. Lozano, R. Garcia, Theory of multifrequency atomic force microscopy, Phys. Rev. Lett. 100 (2008) 076102.
[27] L.N. Kantorovich, T. Trevethan, General theory of microscopic dynamical response in surface probe microscopy: from imaging to dissipation, Phys. Rev. Lett. 93 (2004) 236102.
[28] N. Oyabu, P. Pou, Y. Sugimoto, P. Jelinek, M. Abe, S. Morita, R. Perez, O. Custance, Single atomic contact adhesion and dissipation in dynamic force microscopy, Phys. Rev. Lett. 96 (2006) 106101.
[29] A. Schirmeisen, H. Hölscher, Velocity dependence of energy dissipation in dynamic force microscopy: hysteresis versus viscous damping, Phys. Rev. B 72 (2005) 045431.
[30] N.F. Martinez, W. Kaminski, C.J. Gomez, C. Albonetti, F. Biscarini, R. Perez, R. Garcia, Molecular scale energy dissipation in oligothiophene monolayers measured by dynamic force microscopy, Nanotechnology 20 (2009) 434021.
[31] A. SanPaulo, R. García, Tip–surface forces, amplitude, and energy dissipation in amplitude modulation force microscopy, Phys. Rev. B 64 (2001) 193411.
[32] S. Hu, A. Raman, Analytical formulas and scaling laws for peak interaction forces in dynamic atomic force microscopy, Appl. Phys. Lett. 91 (2007) 123106.
[33] H. Holscher, U.D. Scharwz, Theory of amplitude modulation atomic force microscopy with and without Q-control, Int. J. Non-Linear Mech. 42 (2007) 608.
[34] J. Legleiter, The effect of drive frequency and set point amplitude on tapping forces in atomic force microscopy: simulation and experiment, Nanotechnology 20 (2009) 245.
[35] B.V. Derjaguin, V.M. Muller, Y.P. Toporov, Effect of contact deformation on the adhesion of elastic solids, J. Colloid Interface Sci. 53 (1975) 314.
[36] N.W. Tschoegl, in: The Phenomenological Theory of Linear Viscoelastic Behaviour, Pringer-Verlag, Berlin, 1989.